Biogeosciences, 22, 8093–8111, 2025
https://doi.org/10.5194/bg-22-8093-2025

Biogeosciences Open Access EGU

Multiscale statistical analysis of thermal and non-thermal components of seawater pCO_2 in the Western English Channel: scaling, time-reversibility, and dependence

Kévin Robache and François G. Schmitt

Laboratoire d'Océanologie et Géosciences, Université du Littoral Côte d'Opale, Université de Lille, CNRS, IRD, UMR LOG 8187, 62930 Wimereux, France

Correspondence: Kévin Robache (kevin.robache@univ-littoral.fr) and François G. Schmitt (francois.schmitt@cnrs.fr)

Received: 28 February 2025 – Revised: 13 November 2025 – Accepted: 6 December 2025 – Published: 19 December 2025

Abstract. High-frequency variability of the partial pressure of CO_2 (pCO_2) in coastal environments reflects the complex interplay of physical, chemical and biological drivers. Multiscale statistical approaches provide a robust framework for understanding dynamics across timescales and for reliably assessing coastal carbon processes. In this study, pCO_2 has been measured on the Astan cardinal buoy (Brittany, west coast of France) with at 30 min intervals by Gac et al. (2020), yielding a dataset of 32 582 data points collected over a period of nearly five years. These measurements were then coupled with others of sea surface temperature and salinity, chlorophyll *a*, oxygen saturation and atmospheric pressure. The aim of this study was to consider the statistical properties of the thermal and non-thermal component of pCO_2, based on its relation with temperature established by Takahashi et al. (2009). Using Fourier spectral analysis, it was demonstrated that all marine scalars exhibited scaling properties with power-law slopes ranging from 1.73–1.85 for timescales spanning from 12 h to at least 80–100 d. The results obtained from this analysis indicate a turbulent and intermittent dynamics for all the considered scalars, including sea surface temperature and salinity, chlorophyll *a*, oxygen saturation, pCO_2, and pCO_2 thermal and non-thermal components. A time-reversibility analysis evidenced the irreversibility of the pCO_2 components above 30 d. The irreversibility exhibited by the thermal component was found to be higher than that of the non-thermal component, with an average value of the associated irreversibility index that was approximately 3.5 times higher than that of the non-thermal component over the period of 50–70 d. Furthermore, a methodology known as the Probability Density Function quotient was employed, a method that has not been widely utilized. This approach enabled the identification of values for which there were statistical relationships between variables. This facilitated the quantification of the influence of primary production on the non-thermal pCO_2, or the influence of periods of depression on supersaturation due to atmospheric or terrigenous inputs. This provided new insights into the stochastic coupling between biological and physical processes, when considering high-frequency pCO_2 variability.

1 Introduction

The ocean carbon cycle plays a major role in the global carbon cycle of the Earth. It encompasses a wide array of physico-chemical, biological, and geological processes, each operating at various spatio-temporal scales ranging from the largest to the finest. Examples include extreme events (Yu et al., 2020) and phytoplankton blooms (Bozec et al., 2011). Its significance is crucial for global climate regulation, particularly in light of the pressing issue of global warming. The ocean's role is paramount as it serves as a carbon sink, capable of absorbing approximately 25 % of atmospheric anthropogenic carbon emissions each year, according to recent estimations (Friedlingstein et al., 2023). To anticipate future dynamics of carbon dioxide (CO_2), models serve as valuable tools, such as those used in the Shared Socio-economic Pathways (SSP) scenarios of the Coupled Model Intercomparison Project Phase 6 (CMIP6) used in the Intergovernmental Panel on Climate Change reports (IPCC, 2023). However, constructing and/or improving these models requires in situ observations (Ciais et al., 2014). Time series analysis, in par-

ticular, is needed to assess the multiscale dynamics of monitored quantities. High-frequency time series are therefore essential for constructing reliable models with precise spatial and temporal resolutions. For several years now, efforts are made in this direction to build large observation databases such as the Surface Ocean CO_2 Atlas (SOCAT; Bakker et al., 2016) database, using in part autonomous moorings (Sutton et al., 2014, 2019; Gac et al., 2020). Furthermore, it is really important to record Eulerian (e.g., fixed buoy) or Lagrangian (e.g., drifting buoy) time series to clearly understand the temporal behavior of the marine scalars.

Due to their large variability at all scales, coastal areas are crucial regions to monitor in order to obtain the most accurate carbon balance. These areas are subject to various events having an impact on CO_2 dynamics both in time and space. For example, anthropogenic activities (e.g., industry and agriculture; Northcott et al., 2019), land inputs (Jiang et al., 2013), extreme events (e.g., storms; Crosswell et al., 2014) in these areas are factors of fast CO_2 fluctuations. Furthermore, these zones possess a high seasonality due to different seasonal drivers such as biological activity and sea surface temperature across seasons (Bozec et al., 2011; Marrec et al., 2013; Reimer et al., 2017; Torres et al., 2021). Moreover, these areas can also be particularly turbulent. This can impact the variability across different timescales and the properties of the scalars (e.g., reversibility, scaling properties and intermittency; Zongo and Schmitt, 2011; Schmitt and Huang, 2016; Schmitt, 2023) such as seawater CO_2 (Robache et al., 2025). Hence these zones present a complex multiscale variability which needs to be described and understood as far as possible.

Several studies have shown that thermal variations contribute to fluctuations in the partial pressure of CO_2 (pCO_2) at the seawater surface (Takahashi et al., 1993, 2002, 2009; Wanninkhof et al., 2022). However, as previously mentioned, numerous other physical, chemical, biological, and geological events which are not directly linked to temperature dynamics influence the dynamics of pCO_2. These include processes such as photosynthesis and respiration, as well as air–sea CO_2 exchanges (Gac et al., 2020). The variations in the seawater partial pressure of pCO_2 can thus be classified into two groups: thermal and non-thermal components. In this study, we aim to investigate the dynamics of these two components, and to compare them, using statistical tools from the field of turbulent time series analysis. For this, a coastal database situated in the western English Channel (France) is considered, in order to study an example in a high-variability environment.

The structure of the paper is the following: Sect. 2 presents the data and methods employed in this study, with a detailed description of the approach used to quantify the non-thermal variations of pCO_2 provided in Sect. 2.2. The statistical analysis of these two components is presented in Sect. 3, with a focus on multivariate analysis in Sect. 3.2. Finally, the last sections provide the discussion (Sect. 4) and conclusions (Sect. 5).

2 Data and Methods

2.1 Presentation of the database from the Astan cardinal buoy

The data analyzed here belong to the Astan cardinal buoy, which is situated off the coast of Brittany, France, within the Western English Channel (WEC). Specifically, it is positioned 3.1 km offshore Roscoff (48°44′55″ N and 3°57′40″ W) as depicted in Fig. 1. The WEC is characterized as a turbulent shallow epicontinental sea (Dauvin, 2019). The average depth at the buoy's location is 45 m, and this region experiences pronounced tidal influences, with tidal ranges exceeding 8 m during spring tides (Gac et al., 2020). Consequently, an intense tidal stream is consistently present, facilitating the continuous total vertical mixing of the water column (Pingree and Griffiths, 1978; Reid et al., 1993; Marrec et al., 2013). This buoy is an integral component of the French national observation service COAST-HF, within the IR-ILICO coastal and marine research infrastructure. The seawater surface partial pressure of CO_2 (pCO_2) data were collected on the buoy using a SAMI-CO_2 (Submersible Autonomous Moored Instrument, SunBurst Sensors) sensor, recording measurements every 30 min at 6 m depth. This device monitors pCO_2 by detecting pH changes (via absorbance measures) in a bromothymol blue solution contained within a gas-permeable membrane, induced by the presence of CO_2. Sea Surface Temperature (SST) and Sea Surface Salinity (SSS) were simultaneously measured using a SeaBird Inc. SBE16+ sensor (at 5 m depth), at the same time resolution, and Dissolved Oxygen (DO) and chlorophyll *a* (chl *a*, based on fluorescence and calibrated using low-frequency chlorophyll data; see Gac et al., 2020) concentrations were recorded with a SeaBird Inc. SBE43 sensor and a Cyclops7 sensor (both at 5 m depth), respectively (Gac et al., 2020). To mitigate potential issues related to ambient light, a cover was placed over the fluorescence sensor and the measurements were carried out in an opaque chamber. Oxygen saturation (O_{sat}) was estimated by Gac et al. (2020) following Weiss (1970). Atmospheric pressure (P_{atm}) data were provided by the weather station of the Roscoff Marine Station (at 15 m height).

This database was established by Gac et al. (2020); they assessed the dataset's reliability through a comparison with low-frequency (e.g., weekly) sampling observations with laboratory estimations of pCO_2. Moreover, blank measurements were regularly performed in distilled water for quality control, with sensors retrieved every three months for inspection, cleaning, battery checks, and reagent level verification. More technical details can be found in Gac et al. (2020). The considered database is thus originally composed of six

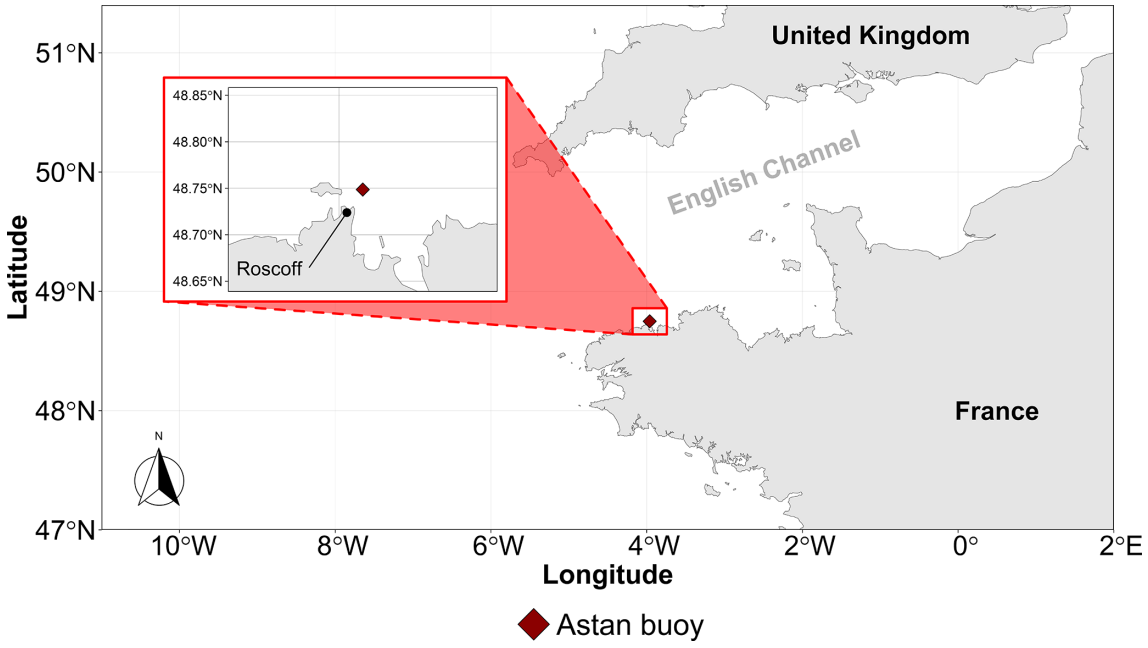

Figure 1. A map of western France indicating the location of the Astan buoy off the coast of the city of Roscoff.

marine and atmospheric parameters (pCO_2, SST, SSS, O_{sat}, chl a, P_{atm}) recorded from 6 March 2015–31 December 2019 with a time step of 30 min. If there were no missing data, the total number of data points would be 84 552. However, due to local failures of the measuring devices, there are missing data for each parameter. Table 1 presents for each parameter the total number of recorded data points, and the associated percentage of missing values: this percentage varies from 19.0 % for P_{atm} to 61.5 % for pCO_2. Due to this large proportion of missing values we are not considering here procedures to fill the gaps. The data analysis methods must then be adapted to time series with large portions of missing values. In addition, the intervals between missing values vary considerably in length, with some being long and others short. As a result, the influence of missing values is distributed across all scales. Overall, despite approximately 60 % of the pCO_2 data being missing, the statistics at each scale (computed from the increments between available values) are still based on a sufficiently large number of observations. Further discussion of this issue, including details on the number of data points at each scale, is provided in Appendix A.

2.2 A non-thermal pCO_2 index

We denote ${pCO_2}^{thermal}$ the changes of pCO_2 induced by temperature changes, under isochemical conditions. This is written as an exponential relation:

$${pCO_2}^{thermal}(T) = A\exp(aT - bT^2)\ , \tag{1}$$

where the parameters classically proposed are the following: $b = 0$ and $a = 0.0423\,°C^{-1}$ based on North Atlantic seawater data (Takahashi et al., 1993); or $a = 0.0433\,°C^{-1}$ and $b = 8.7 \times 10^{-5}\,°C^{-2}$ from a more recent work using a larger dataset (Takahashi et al., 2009). In the present work, we use the latter relation, but we note that the quadratic term is only providing slight corrections to the linear term. The coefficient A is a multiplicative factor that has no influence on the dynamical or statistical properties of ${pCO_2}^{thermal}$. We estimate this value based on the data, as:

$$A = \left\langle \frac{pCO_2(t)}{\exp(aT(t) - bT(t)^2)} \right\rangle\ , \tag{2}$$

where $\langle\cdot\rangle$ means statistical average, performed on the different values in the time series, where t is the time. Figure 2 presents the value of A derived in this study, along with the regression between SST and $\log(pCO_2)$, compared with in situ measurements and the regression reported by Takahashi et al. (1993). When considering the oxygen dynamics in marine waters, one classically divides the oxygen concen-

Table 1. Number of recorded data points (n) and percentage of missing data ($\%_{missing}$) for the time series used for the following of this study.

Scalar	n	$\%_{missing}$
pCO_2	32 582	61.5
Chl a	37 412	55.8
SST	62 981	25.5
SSS	62 475	26.1
O_{sat}	50 752	40.0
P_{atm}	68 463	19.0

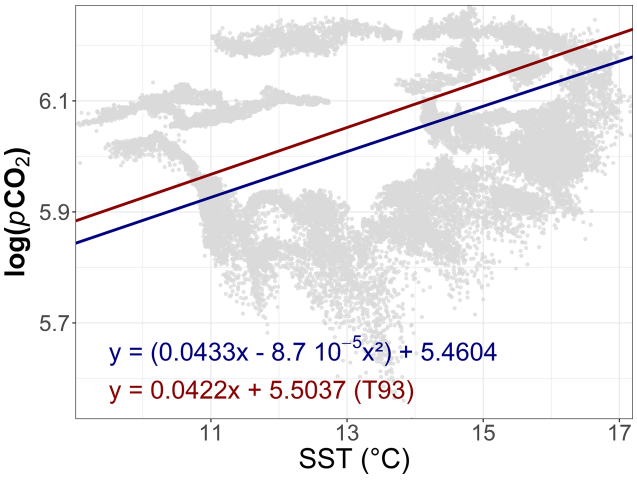

Figure 2. Distribution of the natural logarithm of the pCO_2 data (in µatm) versus the SST (gray points). The empirical linear relation found by Takahashi et al. (1993, T93) is represented by the red line and the red equation. The equation used in this study is represented by the blue line and the blue equation, based on Takahashi et al. (2009).

tration value by the equilibrium oxygen which is a function of temperature and salinity: the ratio is a number without dimension, which is called the oxygen saturation percentage. Inspired by this approach, we consider here the non-thermal dynamics as the ratio X_{sat} between the observed pCO_2 and the thermal component ${pCO_2}^{\mathrm{thermal}}$:

$$X_{\mathrm{sat}} = \frac{pCO_2}{{pCO_2}^{\mathrm{thermal}}} \tag{3}$$

This provides a new time series, where $X_{\mathrm{sat}}(t)$ is a non-dimensional quantity, indicating the saturation of pCO_2; it can be seen as a percentage, and when it is larger than 1 (or 100 %) there is supersaturation, whereas when smaller than 1 there is undersaturation (with respect with an equilibrium value which depends on the temperature).

Let us note that a so-called "non-thermal" component of pCO_2 is often introduced as (Takahashi et al., 1993, 2009; Wimart-Rousseau et al., 2020):

$${pCO_2}^{\text{non-thermal}} = pCO_2 \times \frac{{pCO_2}^{\mathrm{thermal}}(T_{\mathrm{mean}})}{{pCO_2}^{\mathrm{thermal}}(T)} \ , \tag{4}$$

where T_{mean} is the average value of the temperature estimated for a given observation experiment. It can easily be shown using this definition and Eq. (3) that we have ${pCO_2}^{\text{non-thermal}} = \lambda X_{\mathrm{sat}}$ with a proportionality coefficient given by $\lambda = {pCO_2}^{\mathrm{thermal}}(T_{\mathrm{mean}})$, indicating that the classical expression of the non-thermal pCO_2 is proportional to the saturation value X_{sat} which is considered in the present work. Their dynamics are thus the same, but we prefer here to consider the quantity X_{sat} since it is a non-dimensional quantity and its comparison with the value of 100 % directly indicates supersaturation or undersaturation.

2.3 Fourier spectral analysis

Fourier spectral analysis is used to estimate the spectral dynamics of stationary time series. Due to missing data, the classical Fast Fourier Transform (FFT) algorithm, which needs regularly-space data, cannot be used. We therefore use here the Wiener–Khintchine theorem expressing that the spectral energy density is the Fourier transform of the autocorrelation function $C(\tau) = \langle X(t)X(t+\tau)\rangle$:

$$E(f) = \int_{-\infty}^{+\infty} C(\tau)\exp(-2\mathrm{i}\pi\tau f)\mathrm{d}\tau \ , \tag{5}$$

where f is the frequency, and $E(f)$ is the Fourier spectral energy density. The autocorrelation function can be directly estimated on time series with missing values, hence this algorithm is recommended for estimating the spectral dynamics of such time series. We consider here the code described in Gao et al. (2021). The power spectral density is represented in log − log plot in order to emphasize possible scaling regimes of the form $E(f) \sim f^{-\beta}$, where $\beta > 0$ is the spectral exponent. For Brownian motion, $\beta = 2$, and for passive-scalar turbulence (i.e., a scalar that is advected by the flow but does not influence its dynamics) $\beta = 5/3$ (Kolmogorov, 1941; Obukhov, 1949; Corrsin, 1951).

2.4 Time-reversal symmetry

The statistical analysis of time-reversal symmetry allows to assess whether a time series exhibits the same statistical properties when considered in the forward direction of time or in reverse (i.e., by replacing t with $-t$). A time series is considered reversible if its statistical properties remain unchanged regardless of the direction of time. This property was recently studied in the context of turbulence by Schmitt (2023), who observed an increase in time-reversal asymmetry within the inertial turbulent range. This is applied here to *in situ* ocean scalar data, and a time-reversal asymmetry indicator using triple correlations, proposed in the field of statistical physics by Pomeau (Pomeau, 1982, 2004), is used here. This indicator uses the following two triple correlations estimated for a stationary time series u:

$$\begin{aligned} G^+(\tau) &= \frac{\langle u(t)u(t+2\tau)u(t+3\tau)\rangle}{g_3} \ ; \\ G^-(\tau) &= \frac{\langle u(t+3\tau)u(t+\tau)u(t)\rangle}{g_3} \ , \end{aligned} \tag{6}$$

where $u(t)$ is a zero-mean time series, and $g_3 = \langle u^3\rangle$ is a normalization, so that G^+ and G^- are dimensionless quantities. The indicator $\mathrm{Po} = |G^+ - G^-|$, denoted as the Pomeau index (Schmitt, 2023), quantifies the degree of time-reversal symmetry in a series. For a reversible series, where the direction of time does not affect the triple correlations, $\mathrm{Po} = 0$. Conversely, the larger the value of Po, the more the series

is asymmetric by time-reversal. Since Po = 0 for a reversible series, this indicator is also interpreted here as an indicator of irreversibility in the time series. It can be evaluated for different values of the time increment τ, allowing one to examine how irreversibility varies across scales.

2.5 Conditional mean

Conditional means are valuable exploratory tools. They provide a way to estimate the overall, often nonlinear, dynamics of a variable u with respect to another variable v (Wand and Jones, 1994):

$$m(x) = \langle v|u = x\rangle \ , \tag{7}$$

For empirical time series, an interval of values (a, b) can be used instead of a fixed value x in order to estimate the conditional mean:

$$m(x) = \langle v|u \in [a, b]\rangle \ , \quad \text{with } x = \frac{1}{2}(a+b) \tag{8}$$

This approach allows one to capture trends in the conditional dynamics between two variables which can be nonlinear, and cannot, by definition, be captured by a linear regression. The conditional average is usually computed at a given scale (here, over $[a, b]$), so that smaller-scale fluctuations are filtered.

2.6 PDF quotient Q

To analyze the relationship between two random variables, we complement the classical approach of conditional averaging with the Probability Density Function (PDF) quotient method. This method, introduced by Xu et al. (2007), involves estimating the following quotient:

$$Q(x, y) = \log_{10}\left(\frac{P_{u,v}(x, y)}{P_u(x)P_v(y)}\right) \ , \tag{9}$$

where P_u and P_v are the respective PDF of the random variables u and v, and $P_{u,v}(x, y)$ is their joint PDF. This quantity provides insights into the dependence between the two variables in the probability space. Indeed, if u and v are independent, $P_{u,v}(x, y) = P_u(x)P_v(y)$ and so $Q(x, y) = 0$. On the contrary, Q is different from the zero value if a dependence exists. More precisely, $Q > 0$ indicates a positive relation, for which the joint probability density $P_{u,v}(x, y)$ is larger than the product $P_u(x)P_v(y)$ corresponding to the independence between the random variables. Conversely, the values for which $Q < 0$ indicate a "negative" relation, for which the joint probability density is smaller than what would be obtained if the variables were independent.

This provides information that complements what is obtained from the correlation. While the correlation is a single numerical value that quantifies the dependence between two variables for all their values (large or small), the PDF quotient reveals which specific values in the (x, y) plane exhibit strong or weak statistical relationships between the variables.

Table 2. Means (μ), standard deviations (σ) and coefficients of variation (CV $= \sigma/\mu$) for all the time series used in this study.

Scalar (unit)	$\mu \pm \sigma$	CV (%)
pCO_2 (µatm)	416.7 ± 50.1	12.0
X_{sat} (%)	101.0 ± 14.4	14.3
$pCO_2^{thermal}$ (µatm)	409.3 ± 37.1	9.1
Chl a (µg L^{-1})	0.9 ± 0.5	55.6
SST (°C)	13.1 ± 2.2	16.8
SSS (psu)	35.2 ± 0.2	0.6
O_{sat} (%)	102.2 ± 4.8	4.7

3 Results

3.1 Statistical properties of $pCO_2^{thermal}$ and X_{sat} in a turbulence framework

3.1.1 Means and coefficient of variation

The dataset analyzed in this study consists of the original variables given in Table 1 together with the computed series $pCO_2^{thermal}$ and X_{sat}. Hence we consider seven key oceanic scalars: the SST, SSS, chl a, O_{sat}, pCO_2 and associated thermal ($pCO_2^{thermal}$) and non-thermal (X_{sat}) components. First, basic statistical metrics were extracted from these time series, including the mean, standard deviation, and coefficient of variation (CV). These values are presented in Table 2. Most time series exhibit relatively high variability, ranging from 9 %–17 %. However, three time series fall outside this range. Specifically, SSS and O_{sat} show lower variability, with CV values of 0.6 % and 4.7 %, respectively. In contrast, the chl a time series possesses a much higher CV of 55.6 %, largely due to its strong biological seasonality. Its mean concentration is relatively high, close to 1 µg L^{-1}, which is sometimes observed in highly mesotrophic waters (Simboura et al., 2005). The CV of pCO_2 in this study is smaller than that observed for coastal ocean sites (> 20 %) in our previous work (Robache et al., 2025). Nevertheless, it is noteworthy that the X_{sat} time series still exhibits noticeable fluctuations, even in this type of environment.

The database was introduced and analyzed in Gac et al. (2020), where various factors influencing the pCO_2 within the WEC were identified. These include tidal patterns, daily cycles, specific rainfall events, and biological processes such as respiration and photosynthesis. Expanding on this analysis, the study highlighted the multiscale variability of partial pressure of CO_2 in seawater, spanning timescales from six-hour fluctuations to seasonal trends. Based on these results, here we apply other metrics to characterize the dynamics and inter-relations of these time series.

3.1.2 Presentation and distribution of the X_{sat} time series

The time series of X_{sat} is shown in Fig. 3. Notably, this variable does not remain consistently at 100 %, but exhibits fluctuations across various timescales, ranging from hours to years. Values vary from a minimum of 59.4 % in June 2016 to a maximum of 134.7 % in December 2019. The mean value is 101.0 ± 14.4 % with a variation coefficient of 14.3 %. Overall, this indicates that the non-thermal component of pCO_2 exhibits non-negligible fluctuations, reflecting its own dynamics. At large scale, the values seem to present a seasonal dynamics: X_{sat} is larger than 100 % from October 2015–April 2016, from September 2017–February 2018, and from September–December 2019. As already mentioned in Gac et al. (2020), these super-saturated values in winter could be linked with riverine inputs (e.g., from Morlaix and Penzé rivers) and to bacterial respiration. On the contrary, undersaturated X_{sat} values (smaller than 100 %) are found from March–October 2015, from April–October 2016, and from April–September 2019: this corresponds to consumption of CO_2 by the primary production in spring and summer. The PDF of X_{sat} shown in Fig. 4a reflects this seasonal behavior, with peaks between 80 % and 90 % corresponding to primary production, and above 110 % for winter values. Both Fig. 4a and 4b in linear and log-linear plots respectively show that the PDF is non-Gaussian and also non-symmetric. More values and a longer tail were recorded below 100 %: approximately 55 % of the values are below this threshold according to Fig. 4c. However, this result should be interpreted with caution due to the presence of missing data in the series.

3.1.3 Scaling properties

Fourier spectra have been estimated for each series and displayed in Fig. 5 in log − log plots, with the aim of characterizing the dynamics of the time series of the different scalars across temporal scales. Approximate scaling behavior are found visually; in order to estimate precisely the power-law slopes, power-law regressions (i.e., $y = x^{\beta}$) are estimated over the same range of scales for each series, from 1.1 (to avoid the daily cycle influence) to 80 d. The highest frequencies (below the daily scale) are not considered to avoid the effects of missing data and the daily and tidal periodicities, which can disrupt the scaling properties (Schmitt and Huang, 2016). The values of β and their regression standard deviation area provided in Table 3. In most cases the power-law fits estimated over this range of frequency scales extend approximately over low frequencies until the annual time scale. Additionally, distinct peaks were observed linked to tidal cycles ($\approx$ 12.4 h in the WEC), and the daily cycle (especially for chl *a*, Fig. 5d), and annual patterns.

All the slopes are close to the value of 5/3 corresponding to passive-scalar turbulence, with values ranging between 1.73 and 1.85. The shapes of the $pCO_2{}^{thermal}$ (Fig. 5c) and SST (Fig. 5e) spectra appeared very similar, with the same scaling exponents. The scalars which are usually defined as passive scalars (i.e. SST and SSS; Corrsin, 1951) possess here the smallest β values: the spectral slopes for X_{sat}, pCO_2, O_{sat} and chl *a* time series are closer to 1.80. This difference with the theoretical 5/3 value could be explained by a strong small-scale (e.g., from hours to months; Robache et al., 2025) intermittency for these scalars (Frisch, 1995; Seuront et al., 1996). In the turbulence framework, intermittency is an intrinsic property of turbulent time series (Frisch, 1995). Intermittency in turbulence was first revealed through early experimental measurements (Batchelor and Townsend, 1949): the term refers to strong, localized fluctuations in the velocity field, as well as in turbulent scalars. More broadly, this means that extreme fluctuations can be observed across different scales, occurring much more frequently than would be expected for a Gaussian process. To assess this potential effect, we estimate the fraction of small-scale variance arising from fluctuations below the 12.4 h tidal scale, using a 12.5 h moving average. This smoothing procedure reduced high-frequency variability, effectively removing structures with periods shorter than 12.4 h. We then quantified the variance associated with these high-frequency fluctuations by computing the ratio between the variance of the smoothed ($\sigma^2_{smoothed}$) and original (σ^2) time series, expressed as a percentage:

$$\rho = 1 - \frac{\sigma^2_{smoothed}}{\sigma^2} \tag{10}$$

For small values of ρ, the contribution of small-scale variability is limited, whereas larger values of ρ indicate a greater proportion of small-scale fluctuations. As shown in Fig. 6, the steepness of the slope β may be related to the indicator ρ, showing that a relationship emerges between this index of small-scale variability and the value of β.

Table 3. Spectral slopes β estimated for the seven considered parameters, for scales from 1–80 d. The associated spectra are displayed in Fig. 5. Difference between each slope values β and β_{SST} are also given to quantify the difference with the passive scalar slope.

Scalar	β	$\beta - \beta_{SST}$
pCO_2	1.82 ± 0.05	0.09
X_{sat}	1.82 ± 0.04	0.09
$pCO_2{}^{thermal}$	1.73 ± 0.05	0
Chl *a*	1.85 ± 0.08	0.12
SST	1.73 ± 0.04	0
SSS	1.74 ± 0.05	0.01
O_{sat}	1.79 ± 0.05	0.06

3.1.4 Reversibility

Based on the results reported from the Fourier spectral analysis, the dynamics of each of the scalars considered in this

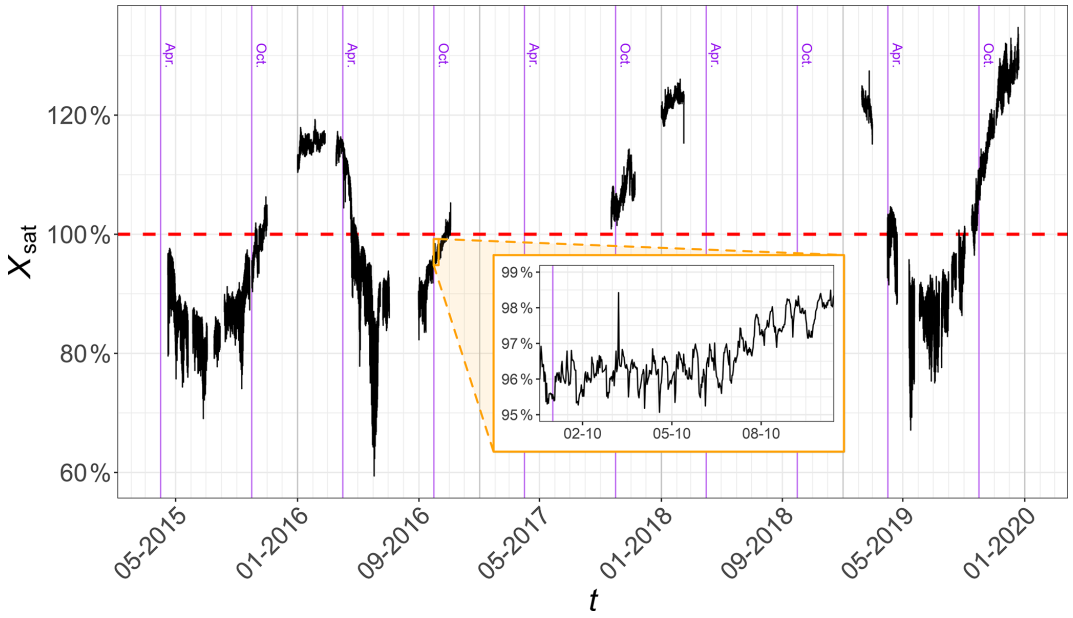

Figure 3. The complete X_{sat} time series, as defined in Eq. (3), represented as a percentage. The red dashed line represents the 100 % value which is reached when $pCO_2 = pCO_2{}^{thermal}$. The inset is a zoom over a period of 10 d showing that the series presents fluctuations even at small scales. Purple horizontal lines indicate April and October of each year, providing quick visual reference points along the x axis, which is spaced at monthly intervals.

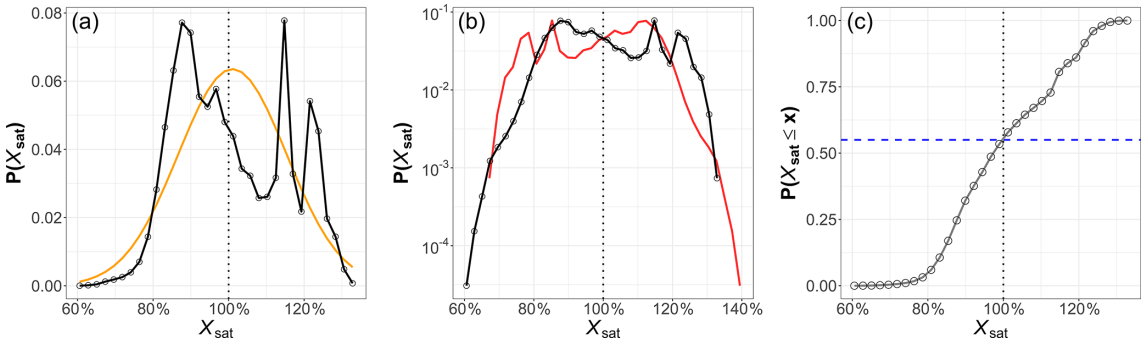

Figure 4. The PDF of X_{sat} time series (%): **(a)** in linear plot, **(b)** in log-linear plot and **(c)** the distribution function. The orange line in **(a)** shows a Gaussian fit with the same mean and variance; the red line in **(b)** represents the symmetric PDF; the vertical dashed line in **(c)** denotes the 100 % value, reached when $pCO_2 = pCO_2{}^{thermal}$ and the horizontal blue line represents the probability $P(X_{sat} \leq 100) = 0.55$. The band width used in **(a)** and **(b)** corresponds to 3 % of the difference between the maximum and minimum values of X_{sat}.

study is considered using tools from the field of turbulence. Recently, the property of irreversibility – essential for characterizing the temporal symmetry of signal statistics – has been investigated in relation to turbulence (Schmitt, 2023). Indeed, in nature many phenomena can be modeled by a nonlinear relaxation dynamics, characterized by a rapid growth phase followed by a slower decay. Examples include epidemic outbreaks (Bestehorn et al., 2022), river discharge (Mathai and Mujumdar, 2022), or El Niño–Southern Oscillation (ENSO; An and Jin, 2004) variability in climatology. The characterization of time-reversal asymmetry in oceanography is thus of relevance in this context. To our knowledge, this type of analysis has never been applied to in situ environmental time series, and the turbulent context here offers a valuable opportunity to explore this property for the series under consideration. Therefore, the reversibility analysis has been applied to all seven time series. An example of triple correlation function G is displayed in Fig. 7 for the SST series only, as an illustration: it is seen that the two functions $G^+(\tau)$ and $G^-(\tau)$ are close for scales τ below 25 d, and after this time scale, the two curves diverge quickly. The corresponding indicator Po has low values below this threshold, indicating a time reversibility for this temporal range, and irreversibility after 25 d, as shown in Fig. 8. In this figure all values of $Po(\tau)$ for scales from 0–70 d are superposed, since this indicator is dimensionless: it corresponds to a quantification of the de-

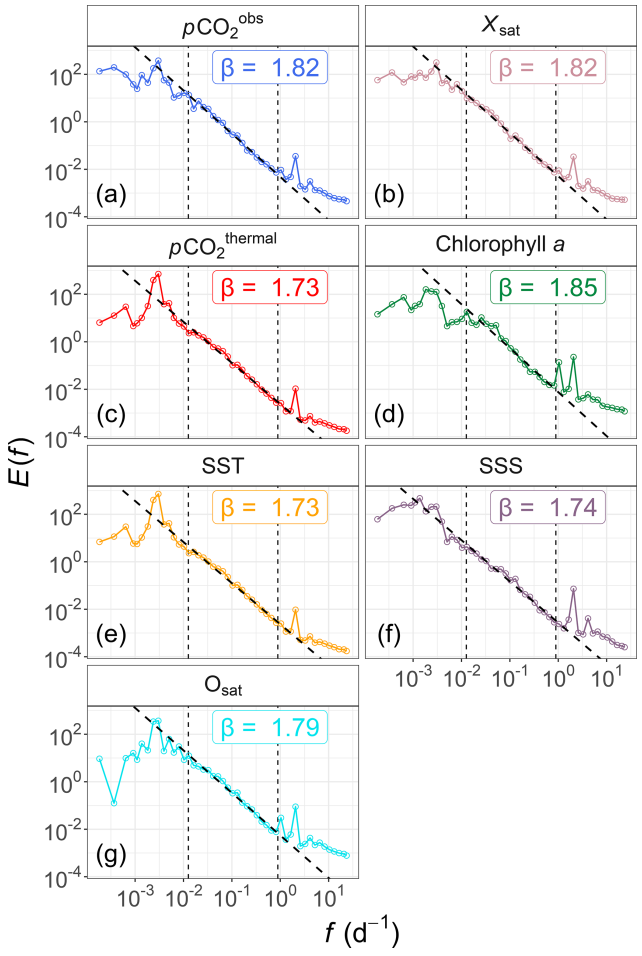

Figure 5. Fourier power spectral analysis, in log − log plots, of seven time series from the Astan buoy: **(a)** pCO_2, **(b)** X_{sat}, **(c)** $pCO_2^{thermal}$, **(d)** chlorophyll *a*, **(e)** SST, **(f)** SSS and **(g)** O_{sat}. The frequencies are expressed in d^{-1}. The black dashed lines represent the power-law regression for each time series, estimated for frequencies from 1.1–80 d. More information about the slopes β associated to these spectra is given in Table 3.

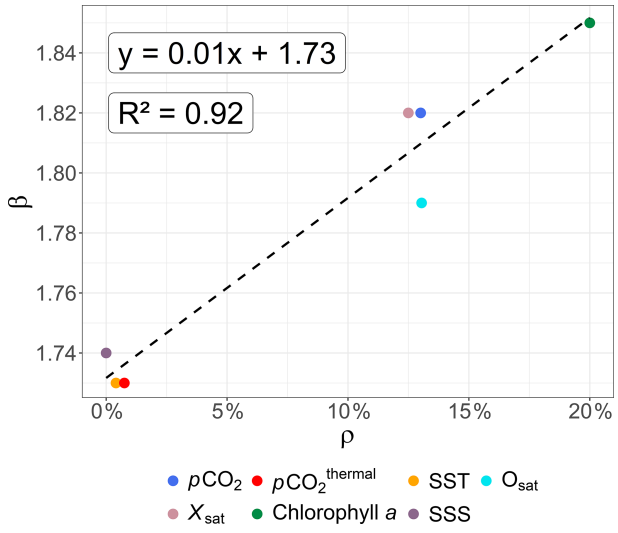

Figure 6. Fourier slope β versus the indicator ρ, representing the influence of high-frequency fluctuations below tidal timescale for each time series. The black dashed line represents a linear regression.

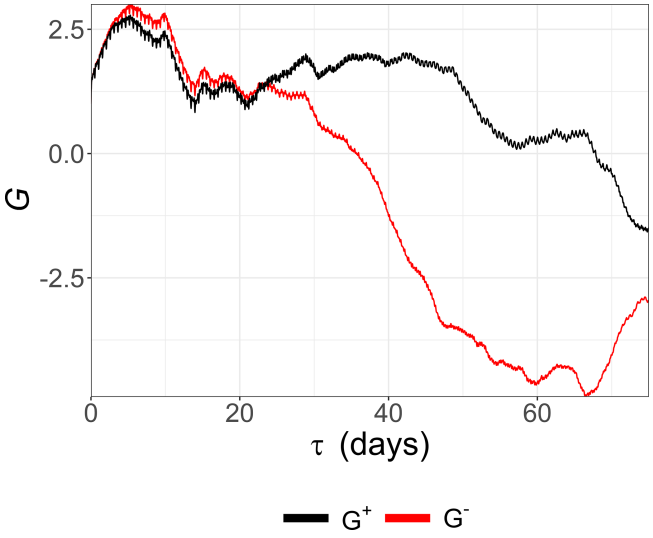

Figure 7. Triple correlation functions $G^+(\tau)$ (black line) and $G^-(\tau)$ (red line) for the SST time series.

parture from 0 of the time-reversal symmetry of each series. We can see that for three series, the curves stays very close to zero at all scales: SSS, chl *a* and O_{sat}. These series may be considered as time-reversal symmetric. For the other series, for scales below 30 d, the indicator remains very small, with values smaller than 2, an arbitrary threshold we have plotted in the figure. It is then increasing and reaching an approximate plateau (with fluctuations) for scales from 50–70 d.

We then consider in Table 4 several values derived from the Po(τ) curves: the time scale τ_{min} corresponding to the first time for which Po(τ) > 2 (for three series this value cannot be extracted since the curve always remains close to zero); the maximal value Po_{max} reached by Po; and $\overline{Po}$, the average value of Po estimated over scales $\tau \in [50; 70]$. This shows that the four series pCO_2, X_{sat}, $pCO_2^{thermal}$ and SST become clearly irreversible for timescales larger than 30–50 d, the larger value $\tau_{min} = 50.7$ is for the X_{sat} time series. Further, Po_{max} as well as $\overline{Po}$ are the larger for the pCO_2 time series, followed by $pCO_2^{thermal}$, SST and X_{sat} in decreasing order. As for the Fourier spectra, it can be seen that SST and $pCO_2^{thermal}$ *Po* time series dynamics are very similar.

In summary, there are two types of dynamics: chl *a*, SSS and O_{sat} are found to be time-reversal symmetric, whereas the other series are time-reversal symmetric for scales below one month, and become irreversible for larger scales, the stronger irreversibility being found for pCO_2 and $pCO_2^{thermal}$.

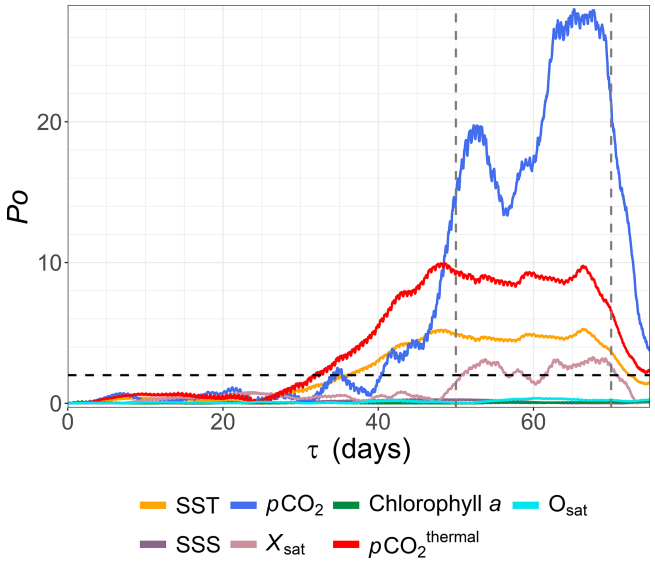

Figure 8. The indicator Po versus τ for all seven time series. The horizontal dashed line represents the value $\mathrm{Po} = 2$. The vertical dashed lines represent the values $\tau = 50$ and $\tau = 70$ d.

Table 4. The minimum value $\tau_{\min}$ for which $\mathrm{Po} > 2$; the maximum value of Po, and the mean $\overline{\mathrm{Po}}$ and standard deviation of Po estimated for $\tau \in [50; 70]$ for each scalar.

Scalar	$\tau_{\min}(\mathrm{Po} \geq 2)$ (d)	$\mathrm{Po}_{\max}$	$\overline{\mathrm{Po}} \pm \sigma$
pCO_2	34.2	28.0	20.9 ± 4.9
$pCO_2{}^{\mathrm{thermal}}$	31.6	9.9	8.8 ± 0.5
SST	36.1	5.3	4.7 ± 0.3
X_{sat}	50.7	3.0	2.5 ± 0.5
Chl a	–	0.2	–
SSS	–	0.3	–
O_{sat}	–	0.4	–

3.2 Multivariate statistics

In the previous sections, we focused on the univariate statistical properties of the scalars. In this section, we turn to the statistical relationships that may exist between different scalars, using a range of methods, some more common than others, with the aim of characterizing them.

3.2.1 Conditional means

In this Section and the following the focus is directly on the behavior of X_{sat}. We consider here first the conditional means of X_{sat} with respect to the values of other variables, to visualize the interactions between variables. They are displayed in Fig. 9. First, three plots show a direct and clear relation. There is as expected a direct relation between pCO_2 and X_{sat} visible in Fig. 9d. Further, a clear relation is also observed between the chl a concentration and X_{sat} in Fig. 9e: an increase in the former is linked with a decrease in the latter. The same relation is observed in Fig. 9f, suggesting that it may be the effect of primary production.

Furthermore, a link between X_{sat} and SSS is also noted, however less clear for large values of SSS, in Fig. 9b: low salinity values are linked to high values of X_{sat}. A similar relationship is found with atmospheric pressure P_{atm} in Fig. 9c: large values of X_{sat} are found in case of atmospheric depressions. These two observations suggest an effect of rainfall events and/or river discharges, which impact pCO_2. This quantitatively confirms what was visually mentioned in Gac et al. (2020).

Finally, a link is also found between SST and X_{sat} in Fig. 9a. This observation may seem counterintuitive due to the definition of X_{sat}, in which pCO_2 is corrected from direct temperature influences. However, the pattern in Fig. 9a can be explained by indirect influences: on the one hand, there is the annual seasonality of SST and on the other hand, there are different seasonal processes impacting pCO_2 without having a direct link with temperature dynamics, such as phytoplankton blooms during spring or notable rainfall events and storms during autumn and winter. Moreover, this association is primarily linked to the seasonality of biological activity, as demonstrated in Fig. 10. Indeed, the two time series presented in Fig. 10a appear to have an opposite dynamics: their Pearson correlation yields a value of -0.84 (with a p value $\approx 1 \times 10^{-12}$). The monthly seasonality is also depicted in Fig. 10b, where the two time series appear to have seasonal averages that are clearly related through a seasonal elongated lemniscate (i.e., a curve shaped like a figure eight or an infinity symbol).

3.2.2 PDF quotient $Q(x, y)$

In this Section, the statistical relations of X_{sat} with other parameters is considered using the PDF quotient method. As explained in Sect. 2.6, the correlation (or covariance) between two series provides only a single number, without accounting for how both variables may be related across their range of variation. Here, the PDF quotient makes it possible to identify the ranges of values over which the scalars are more or less dependent on each other, and the strength of this dependence. The results are presented in Fig. 11, with blue and red colors for negative and positive values of $Q(x, y)$, respectively. Let us recall here that regions for which $Q > 0$ indicate values for which there are strong statistical relationships between the variables and when $Q = 0$ there are no statistical relations between the variables. Low values of Q are emphasized by gray zones (for which $|Q| < 0.3$). They correspond to an lack of statistical relationship as found for a large part of the panel (c) for atmospheric pressure, or of panel (b) for SSS. On the contrary red values show large relationships. Table 5 shows the minimum and maximum values of the PDF quotient for each parameter. This range shows that the minimum values are close for each parameter, and that the maximum values is much larger for pCO_2, chl a

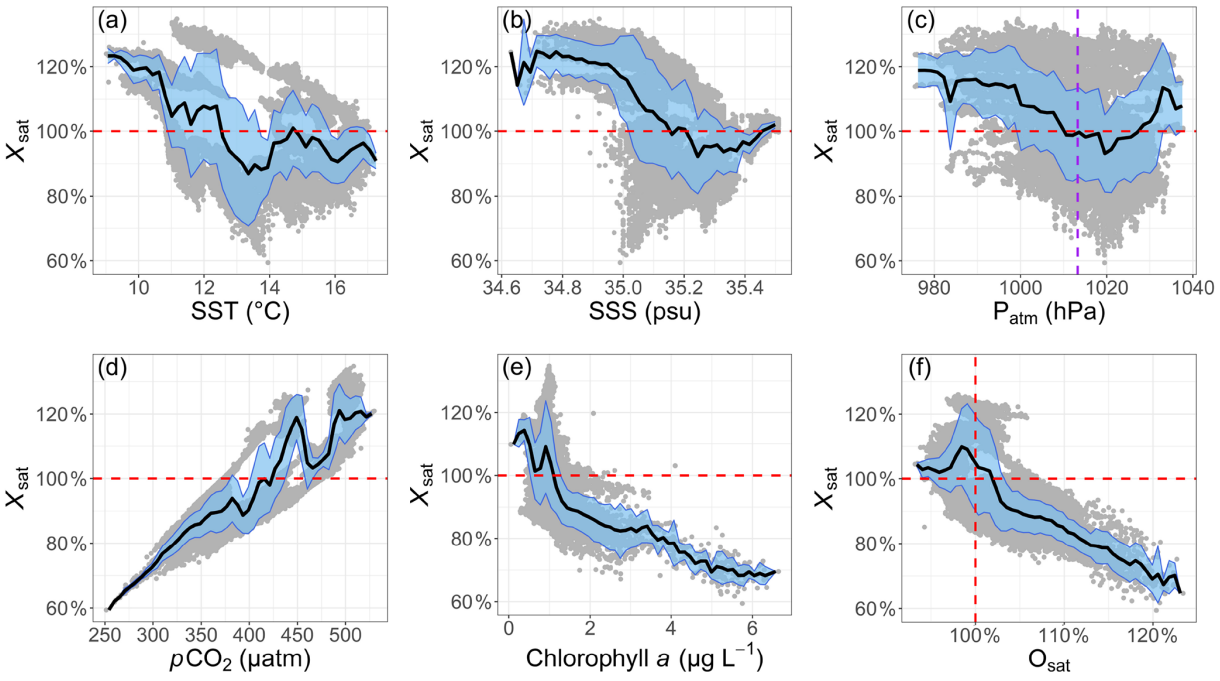

Figure 9. Conditional means of $X_{sat}(t)$ with respect to several other variables: **(a)** SST, **(b)** SSS, **(c)** atmospheric pressure P_{atm}, **(d)** pCO_2, **(e)** chlorophyll *a* and **(f)** oxygen saturation O_{sat}. The blue area represents the standard deviation calculated for each range. The red vertical dashed lines – and the horizontal one in panel **(f)** – represent the 100 % value. The purple vertical dashed line in panel **(c)** represent the mean atmospheric pressure at mean sea level (1013.25 hPa). For each variable, the chosen bandwidth b_w used for the calculation of the conditional mean is defined as 2 % of the difference between its maximum and minimum values. The *x*-value is the mean of each bounds of each range.

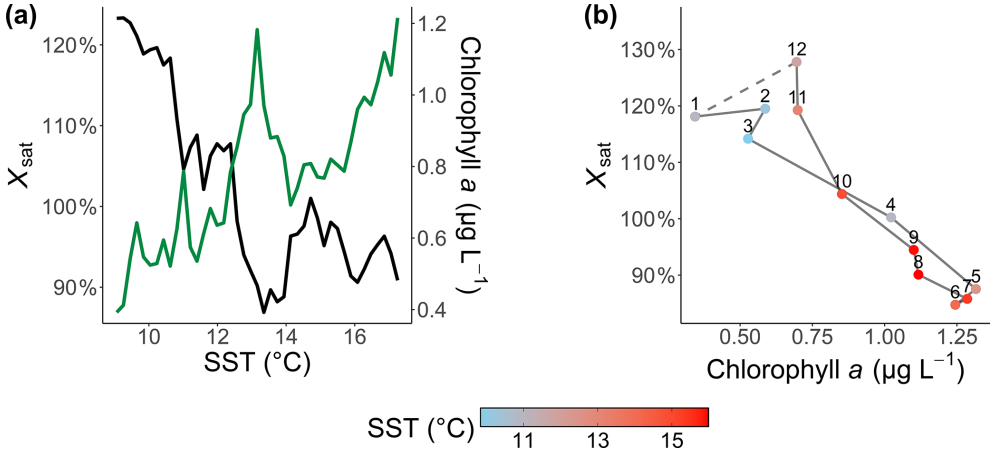

Figure 10. Illustration of the link between X_{sat} and the seasonality of the chlorophyll *a*: **(a)** conditional means of chlorophyll *a* (green line) and X_{sat} (black line) versus the SST (as in Fig. 9) and **(b)** mean X_{sat} versus the mean chlorophyll *a* (black line). The color of the dots indicates the mean SST for each month of the year themselves indicated by numbers (1 for January, 12 for December).

and O_{sat} (with values from $10^{4.1} \simeq 12\,600$ to $10^{4.5} \simeq 31\,600$) than for SST, SSS or P_{atm} (with values from $10^{2.1} \simeq 125$ to $10^{2.3} \simeq 200$). Such large values indicate a strong statistical relationship. More comments are provided below as related with the values of X_{sat}.

We first consider the half-plane for which $X_{sat} < 100\,\%$: panel (e) shows that large Q values are observed for large chl *a* ($> 2\,\mu g\,L^{-1}$) and low X_{sat} values ($< 85\,\%$), and panel (f) similarly that large Q values are found for large O_{sat} ($> 110\,\%$) and low pCO_2 ($< 350\,\mu atm$) values. This corresponded to phytoplankton bloom periods, during which low X_{sat} values are reached due to CO_2 consumption associated with photosynthesis: the PDF quotient method is a way to provide a quantification that confirms visual observations.

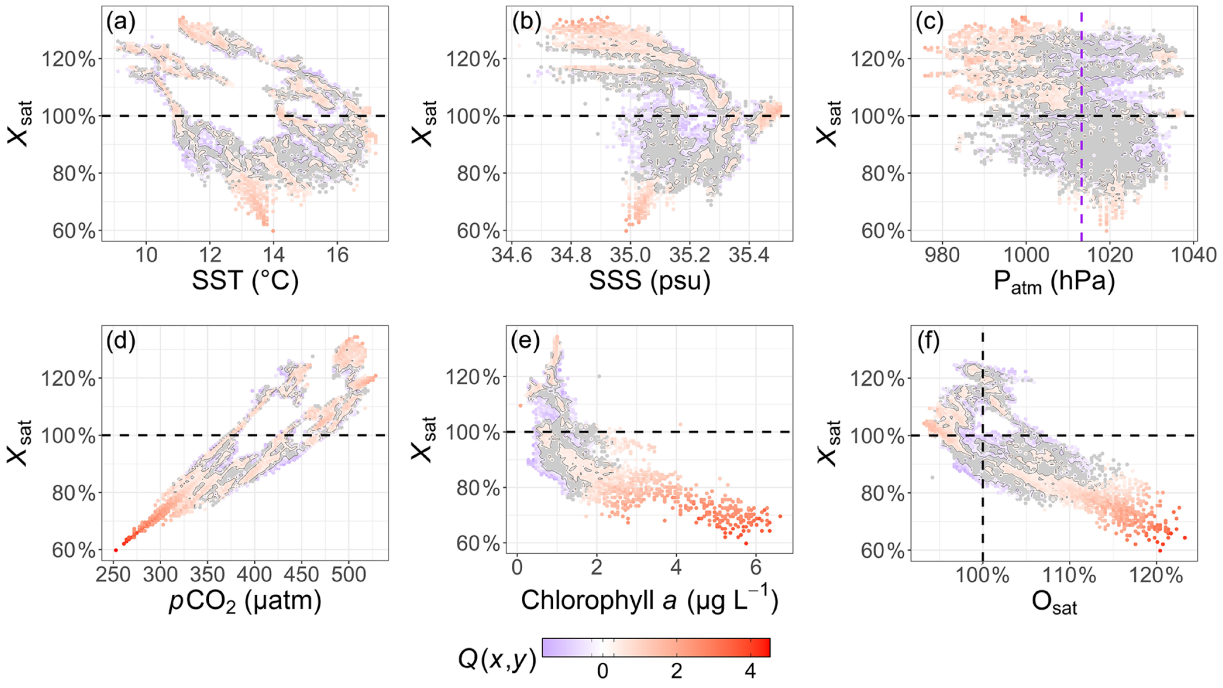

Figure 11. Representation of the PDF quotient $Q(x, y)$ estimated for X_{sat} and **(a)** SST, **(b)** SSS, **(c)** atmospheric pressure P_{atm}, **(d)** pCO_2, **(e)** chlorophyll a and **(f)** oxygen saturation O_{sat}. The horizontal black dashed lines – and the horizontal one in panel **(f)** – represent the 100 % value. The vertical purple dashed line in panel **(c)** represents the mean atmospheric pressure at mean sea level (1013.25 hPa). For each variable, the chosen bandwidth used for the calculation of the 2D-PDF is defined as 1 % of the difference between its maximum and minimum values. The x value and y value are the mean of each bounds of each range. A contour plot of the value $|Q| = 0.3$ is represented in each panel and the value below this threshold are represented in gray, to separate visually the area where $10^{|Q|} < 2$.

Table 5. The minimum and maximum values of the PDF quotient Q for each scalar in comparison to X_{sat}.

Scalar	Q_{min}	Q_{max}
SST	−1.3	2.1
SSS	−1.4	2.2
P_{atm}	−1.2	2.3
pCO_2	−1.6	4.5
Chl a	−1.6	4.1
O_{sat}	−1.5	4.2

The links between chl a and X_{sat} are more complex for values below 2 µg L^{-1}, with Q values closer to 0. In some cases, a "negative" relation ($Q < 0$) can even be found. More globally, an independency ($Q = 0$) or a lower relation ($|Q| < 1$) was more often observed for this range of chl a values, which are more often recorded referring to the associated joint probabilities (97 % of the chl a recorded values).

For intermediate values of X_{sat} (between 85 % and 115 %, representing 64 % of recorded data), the patterns are often mixed. The mean values of Q for this X_{sat} range of values were globally all smaller than 1 and even close to zero in some cases, e.g. with chl a for X_{sat} values ranging between 100 % and 105 % (Fig. 11e). This is especially true between 85 % and 95 %, where no clear link is observed with any other scalar, visible by the gray zones in the figures. For X_{sat} values between 95 % and 105 %, larger values of Q are found for $O_{sat} < 95$ %.

Finally, let us consider large values of X_{sat} (> 115 %), for which large Q values are observed for the lower part of the SSS values (below 35 psu) in panel (b), and below 1000 hPa for the pressure in panel (c). The two observations are consistent and indicate that supersaturation of X_{sat} corresponds to a depression with lower values of salinity due to rainfall or riverine inputs. In panel (a) the lower temperatures associated with large values of Q indicate that such events happen in winter. Here also the PDF quotient approach helps to quantify relationships and to provide a quantitative justification of proposed mechanisms.

4 Discussion

The time series recorded on the Astan cardinal buoy have been used to study the statistical properties of several marine scalars, of which the thermal and non-thermal components of the seawater partial pressure of CO_2. First, a quantity, X_{sat}, was proposed in Eq. (3), similar to $pCO_2^{non\text{-}thermal}$ found in the literature (Takahashi et al., 1993, 2009; Wimart-Rousseau et al., 2020) but proportional to it. The advantage

of using X_{sat} is that it provides a pCO_2 saturation percentage, allowing for the direct identification of sources (supersaturation) or sinks (undersaturation). For the database studied here, X_{sat} primarily ranges between 80 (5th percentile = 81 %) and 120 % (95th percentile = 124 %).

In this work, we focused on X_{sat} and its relationship with other measured quantities. All marine quantities studied are influenced by turbulence, exhibiting scale-invariant statistics with a spectral exponent β close to 5/3 (Fig. 5) over timescales ranging from 12 h to at least 80–100 d. In certain time series, annual, daily, and especially tidal forcing were evident. For some series, the β values were larger than the 5/3 Kolmogorov–Obukhov–Corrsin passive scalar value corresponding to non-intermittent turbulence. This has already been found for SST and chl *a* in a previous study in the eastern English Channel (Seuront et al., 1996). The slightly steeper slopes found for some series could be related with the intermittency, as supported by the link observed between the importance of the high-frequency fluctuations, below the tidal forcing timescale ($\simeq$ 12.4 h) on the scalar dynamics and the associated β values found (Fig. 6). Remarkably, the 5/3 slope was also observed for X_{sat}. This indicates that even without thermodynamic effects, oceanic pCO_2 dynamics in the western English Channel (WEC) remains influenced by turbulence. This result differs from our previous study, where we found a mean power-law slope of 1.47 for coastal seawater time series (Robache et al., 2025). This discrepancy could be attributed to the strong hydrodynamic forcing in the present dataset, primarily driven by the macrotidal dynamics of the WEC (tidal range > 4 m; Levoy et al., 2000; Idier et al., 2012).

Despite these similarities in spectral slopes, the time series exhibit different dynamics, as revealed by the reversibility analysis through the time reversal symmetry analysis. Interestingly, quantities more closely linked to biology, such as O_{sat} and chl *a*, and even SSS, are reversible, despite their otherwise turbulent dynamics. Other quantities are reversible at small scales and become irreversible at timescales greater than 30 d. At these larger timescales, we found that the most irreversible signals are those of pCO_2 and $pCO_2{}^{thermal}$. The quantity X_{sat} exhibits an intermediate behavior between SST, pCO_2, and the reversible variables, as if accounting for the direct effects of temperature had brought it closer to biological dynamic. The fact that some series become irreversible at scales larger than 30–50 d could be related to climate forcing. Indeed, irreversibility in climate time series has already been observed by Giancaterini et al. (2022). Moreover, we applied Empirical Mode Decomposition, an algorithm that extracts modal fluctuations from a time series (Huang et al., 1998), to SST (not shown here). This analysis revealed that irreversibility may be associated with large-scale modal fluctuations, including those with periods of one year or longer.

The relation between variables have been investigated for X_{sat}, with the conditional mean and Probability Density Function (PDF) quotient methods. The conditional means, and especially the PDF quotients, have made it possible to quantify the observation first made visually on the X_{sat} series. For low values of X_{sat}, the conditional mean, as well as the PDF quotient, showed that these values are associated with high values of chl *a* and O_{sat}, showing that they are associated with photosynthesis and primary production at temperatures between 12 and 14 °C. High X_{sat} values are often associated with low atmospheric pressures, lower SSS values (visible through the PDF quotient) and, for some of them, lower temperature values (< 12 °C). This indicates that these supersaturation episodes are found during depressions associated with rainfall (atmospheric inputs) and rivers. Another interesting result was the finding of a indirect effect of SST on X_{sat}, due to the links between SST and other parameters influencing the non-thermal component of CO_2 such as chl *a*. The PDF quotient is a novel methodology that was proposed in the past (Xu et al., 2007), yet it has received limited utilization since its inception. In this study, we have employed the PDF quotient method in a systematic manner to augment the conventional bivariate conditional mean analysis. The PDF quotient approach has enabled us to identify the values in the (x, y) space of the variables under investigation where the statistical relationship is most robust. This approach is also noteworthy for its ability to highlight areas in the (x, y) space where statistical independence exists, i.e. values of Q close to zero, as illustrated in gray in Fig. 11. For example, it is evident from Fig. 11 that atmospheric pressure shows no correlation with X_{sat}, except in one quadrant where X_{sat} has high values and simultaneously the pressure is low, as illustrated in panel (c). This also shows that salinity exhibits no relationship with X_{sat}, except in areas of low salinity and high X_{sat} values, as shown in panel (b). Furthermore, it can also be seen that when X_{sat} assumes slightly undersaturated values (between 90 % and 100 %), all the figures corresponding to the PDF quotient associated with different quantities are grayed out, indicating that the PDF quotient approaches zero for these values of X_{sat}. This observation demonstrates that these slightly undersaturated non-thermal pCO_2 values exhibit no discernible relationship with any variable; the underlying causes are multifaceted, and no single parameter appears to be determinative. This is in contrast to the behavior observed for low or very high trans values of X_{sat}, as previously discussed.

The methodological framework used in this study highlights the importance of advanced statistical tools for analyzing fixed-point time series, particularly in highly non-linear and turbulent environments such as WEC. The combination of spectral, time-reversal symmetry, and conditional dependence (conditional means and PDF quotient) analysis has allowed us to study and better understand the complex and scale-dependent dynamics of several scalars and of their relation. The non-linear nature of oceanic pCO_2 dynamics is evident in the interplay between physical, chemical and biological processes, which influence the variability of X_{sat} and $pCO_2{}^{thermal}$ in a non-linear way across different timescales.

Nevertheless, given the 5 year length of the dataset and the presence of gaps, our analysis is best suited to characterizing sub-annual variability and its drivers. The statistics reported here may depend on the forcing associated with interannual variability and its potential anthropogenic forcing. Further analyses, performed over different periods of time, will be needed in future works, in order to compare with the results presented here. Also, longer continuous time series would be required to extend these analyses to larger temporal scales for which other dynamics could be expected (e.g., long-term memory at decadal timescale; Séférian et al., 2013). It is also necessary for these time series to be as temporally homogeneous as possible (i.e., with no or few interruptions) in order to enhance the robustness of the applied statistical analyses. Indeed, in the present case, although each time scale is represented by sufficient statistics, the data are not fully homogeneous on a monthly basis. Appendix A shows that December and March were undersampled compared with other months. At the seasonal scale, however, the distributions are more balanced. This temporal heterogeneity represents one limitation of our analysis and highlights the need for future comparisons with datasets containing fewer missing values. Appendix B examines the effects of missing data on the analysis of PDF quotients, restricting the computation to observations for which all parameters were simultaneously available. The influence of missing values is limited in this case, and the results are broadly consistent with those presented in the main analysis.

This study also underscores the necessity of considering non-linear dynamics and interactions when analyzing air–sea CO_2 fluxes and identifying source-sink dynamics, as the dynamics of ΔpCO_2 is highly linked to oceanic pCO_2 (Robache et al., 2025). The emergence of different behaviors at various temporal scales – such as reversibility at small scales and increasing irreversibility beyond 30–50 d – suggests that deterministic and stochastic influences act differently across timescales in the WEC carbon cycle. This confirms the complex nature of oceanic carbon dynamics and fluxes and underscores the necessity of high-frequency, robust statistical analyses to fully capture and understand them.

5 Conclusions

Fixed-point measurements, collected via high-frequency buoys, are of critical importance for the study of coastal marine dynamics. They also provide a theoretical framework for interpreting fluctuations, as demonstrated here through the application of Eulerian turbulence. For this, high frequency is necessary in order to access the dynamics at small scales, a necessity due to the presence of strong multiscale fluctuations in the systems under study. In this context, a novel quantity, designated X_{sat}, was considered, with its properties evaluated in relation to the other variables. This quantity directly allows pCO_2 of the direct thermal part to be corrected, and highlights periods of supersaturation or undersaturation linked to non-thermal events. We were thus able to highlight here the influence of turbulence on the different parameters, including the X_{sat} quantity, for scales between 1 and 80–100 d. Our results also highlight a marked irreversibility in pCO_2 time series above 30 d, suggesting the influence of non-stationary and dissipative processes, likely linked to underlying oceanic and atmospheric dynamics. This temporal turbulent and asymmetric dynamics has implications for pCO_2 modeling and forecasting, emphasizing the need for approaches that account for irreversible fluctuations and turbulent transport mechanisms in the ocean and atmosphere.

In addition, we explored the potential of a little-known method, the PDF quotient, which makes it possible to identify values for which variables have statistical relationships between them. This enabled us to quantitatively analyze visual observations, such as the influence of primary production on the value of X_{sat} (for X_{sat} below 85 %), or the influence of periods of depression on supersaturation (for X_{sat} above 115 %) due to atmospheric or terrigenous inputs. This method provided new insights into the stochastic coupling between biological and physical processes, reinforcing the importance of considering both drivers when interpreting high-frequency pCO_2 variability. Furthermore, this analysis confirms the complex relationship between pCO_2 and other variables considered as its drivers, such as chlorophyll *a* which can serve as a proxy for the biological carbon pump, emphasizing the need for deeper investigations into their statistical causal relations.

Finally, the findings of this study have direct potential applications in oceanographic monitoring and carbon cycle research. The methodology developed here enhances the accuracy of oceanic pCO_2 dynamics analysis, providing a more precise characterization of high-frequency variability. This improved characterization contributes to a better understanding of coastal biogeochemical processes across multiple temporal scales–an essential step, for example, toward verifying and improving model-based forecasts.

Appendix A: About the missing data problem

Most of the analysis methods employed in this study account for the issue of missing values, a common problem when working with high-frequency in situ observations. For instance, spectral analysis, time-reversal symmetry analysis, and the PDF quotient of increments all incorporate the temporal variability of pCO_2 by considering differences between observations separated by a given time scale τ. This approach ensures that, despite occasional data gaps – sometimes extending over relatively long periods – a sufficient number of samples remains available at each time scale. Figure A1 illustrates the number of pCO_2 increments available for all considered scales between 30 min and 365 d. Despite approximately 60 % missing data in the time series (the highest rate

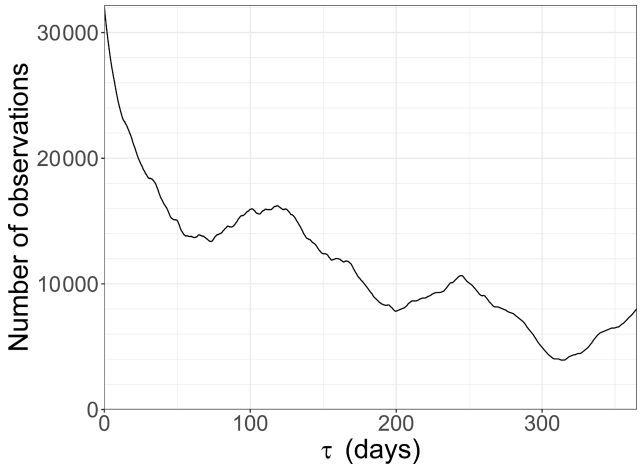

Figure A1. Number of observed temporal increments of pCO_2 as a function of the considered timescale τ.

among our variables; Table 1), more than 3900 temporal increments are available for timescales shorter than one year. This provides sufficient statistical support for our analyses, which rely predominantly on mean values and are restricted to these timescales.

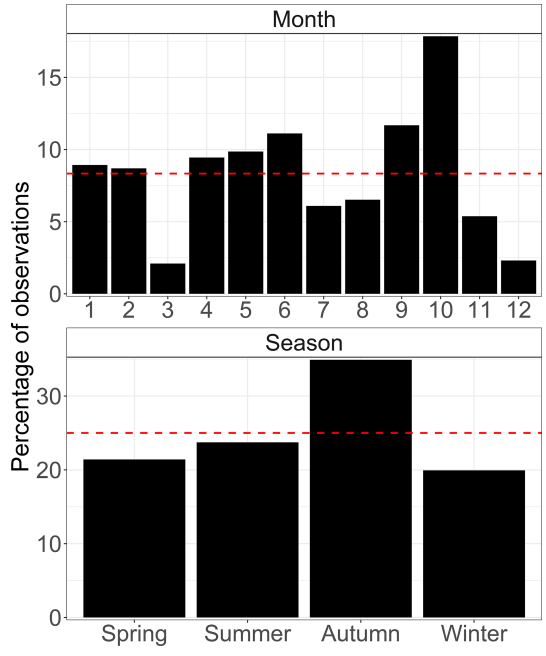

Figure A2. Distribution of the available pCO_2 data by month and season. The red dashed line represents the expected values for a uniform sampling.

On the other hand, the distribution of the available pCO_2 data over the five-year period, shown as a function of month and season in Fig. A2, is not perfectly homogeneous. Some months, such as December and March, are undersampled relative to others, which likely results in an underrepresentation of their dynamics in the aggregated statistics. At the seasonal scale, the distribution is more balanced, although autumn contributes proportionally more data than the other seasons. This sampling structure should be considered when interpreting the results. A full assessment of its influence would require a continuous time series covering the entire period.

Appendix B: Testing the effect of missing data on the PDF quotient analysis

In the analysis presented in Sect. 3.2.2, the numbers of value pairs used to estimate the PDF quotients are not all equal, due to the fact that the missing data are not the same for all series. To verify the robustness of our results, we therefore compared these results with those obtained by considering only the observations for which all parameters were simultaneously present (no missing data in any of the parameters). First, a comparison of the number of pairs used for each parameter in both cases is presented in Table B1. In the case where only simultaneous observations of all scalars are retained (case B in the table), the number of available observations decreases due to missing data for chl a and O_{sat}. These missing values do not occur at the same periods, which explains this reduction. We examined the monthly distribution of the available data pairs in each case. The results are shown in Fig. B1. Panel (a) corresponds to case A. For this case, the distribution of data pairs of SST, chl a, and O_{sat} with X_{sat} is provided. It is not shown for the other scalar variables since their distributions are similar to that of SST. Notably, in case A, most months are covered for all scalars except for O_{sat}, for which December is missing. However, the temporal coverage is not completely uniform at the monthly scale. It is somewhat more consistent at the seasonal scale. For instance, during winter, the values from January and February allow winter conditions to be represented in the results. For case B, shown in panel (b), the distributions are overall similar to those obtained previously for chl a and O_{sat}, except for November and December, when very few values are retained due to the homogenization of the time series across the different scalars (as explained earlier).

Table B1. Number of pair values used to estimate the PDF quotient (compared with X_{sat} values) for each scalar, either by retaining all available pairs (case A) or by considering only the values for which simultaneous measurements of all scalars were available (case B).

Scalar	Case A	Case B
SST	32 582	18 292
SSS	32 582	18 292
P_{atm}	32 582	18 292
pCO_2	32 582	18 292
Chl a	23 238	18 292
O_{sat}	26 480	18 292

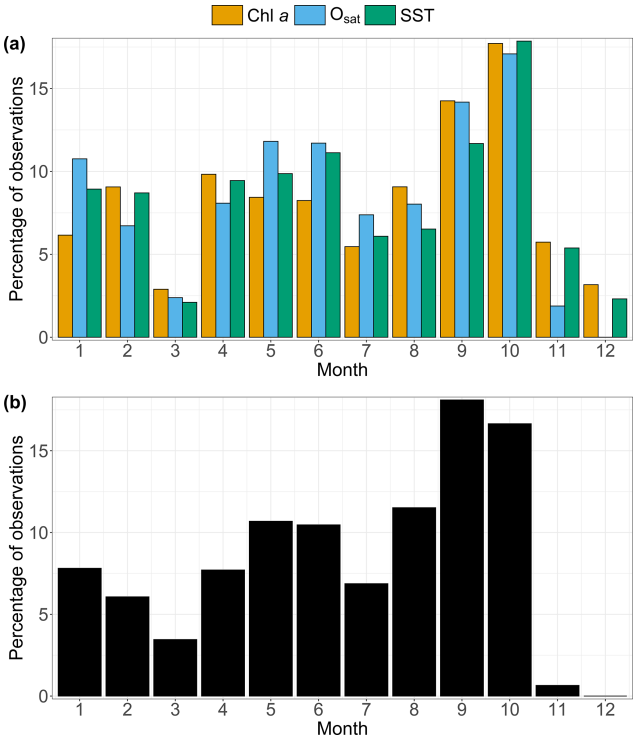

Figure B1. Percentage of observations (%) per month of the year, considering **(a)** all available X_{sat} data (case A) and **(b)** only the subset of data with complete observations for all scalars (case B).

Following this, we repeated the PDF quotient analysis, this time considering only the values recorded simultaneously. The results obtained for SSS and chl *a* are presented in Fig. B2. Overall, the results from this analysis remain consistent with those obtained in Sect. 3.2.2. A relationship is still observed between high X_{sat} values and SSS, as well as between high chl *a* values and low X_{sat} values. The results for the other scalars are not shown here for readability, but the conclusions remain the same for each of them.

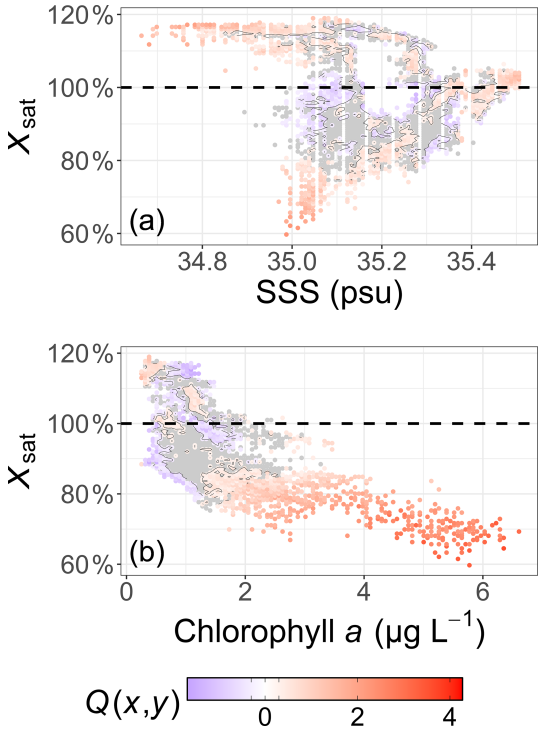

Figure B2. Representation of the PDF quotient $Q(x, y)$ estimated for X_{sat} and **(a)** SSS and **(b)** chlorophyll *a*, using only the data for which all scalars were measured simultaneously (case B). The horizontal black dashed lines represent the 100 % value. For each variable, the chosen bandwidth used for the calculation of the 2D-PDF is defined as 1 % of the difference between its maximum and minimum values. The x value and y value are the mean of each bounds of each range. A contour plot of the value $|Q| = 0.3$ is represented in each panel and the value below this threshold are represented in gray, to separate visually the area where $10^{|Q|} < 2$.

Finally, by relying on a smaller number of observations, some important information is actually lost regarding the interaction between SSS and X_{sat} (and similarly for atmospheric pressure and SST), for which more values are available (i.e., all X_{sat} values). For this reason, in this study we retained in the main text the analyses that included the largest number of values.

Code and data availability. The used database was provided by Gac et al. (2020) (https://doi.org/10.3389/fmars.2020.00712), and is published in Bozec et al. (2025) (https://doi.org/10.17882/106537) and Robache and Schmitt (2025) (https://doi.org/10.17882/106550). The Python code for the Fourier spectral analysis is based on Gao et al. (2021): https://github.com/lanlankai/Scaling-Analysis-of-the-CFOSAT-Along-Track-Wind-and-Wave-Data (last access: 11 September 2025). The R code for the PDF quotient analysis has been published here: https://github.com/KevinRobache/PDF_Quotient_Code (last access: 11 September 2025). All the plots have been made using the "ggplot2" (https://doi.org/10.32614/CRAN.package.ggplot2; Wickham et al., 2025), other "tidyverse" (https://doi.org/10.32614/CRAN.package.tidyverse; Wickham et al., 2019; Wickham and RStudio, 2023), and "ggmagnify" (https://github.com/hughjonesd/ggmagnify, last access: 17 September 2025; Hugh-Jones, 2023) R packages.

Author contributions. KR performed the code and the analysis under the supervision of FGS. KR wrote the first draft and both authors edited and reviewed the final version.

Competing interests. The contact author has declared that none of the authors has any competing interests.

Disclaimer. Publisher's note: Copernicus Publications remains neutral with regard to jurisdictional claims made in the text, published maps, institutional affiliations, or any other geographical representation in this paper. While Copernicus Publications makes every effort to include appropriate place names, the final responsibility lies with the authors. Views expressed in the text are those of the authors and do not necessarily reflect the views of the publisher.

Acknowledgements. The French Région Hauts-de-France and the ANR project CO_2Coast (principal investigator Hubert Loisel, grant no. ANR-20-CE01-0021) are acknowledged for cofunding of the PhD thesis of Kévin Robache. Yann Bozec, Sarah Bureau, and Jean-Philippe Gac are acknowledged for their assistance regarding the technical aspects of the Astan buoy.

Financial support. This research has been supported by the Agence Nationale de la Recherche (grant no. ANR-20-CE01-0021) and the French region Hauts-de-France.

Review statement. This paper was edited by Liuqian Yu and reviewed by two anonymous referees.

References

An, S.-I. and Jin, F.-F.: Nonlinearity and Asymmetry of ENSO, J. Climate, 17, 2399–2412, https://doi.org/10.1175/1520-0442(2004)017<2399:NAAOE>2.0.CO;2, 2004.

Bakker, D. C. E., Pfeil, B., Landa, C. S., Metzl, N., O'Brien, K. M., Olsen, A., Smith, K., Cosca, C., Harasawa, S., Jones, S. D., Nakaoka, S., Nojiri, Y., Schuster, U., Steinhoff, T., Sweeney, C., Takahashi, T., Tilbrook, B., Wada, C., Wanninkhof, R., Alin, S. R., Balestrini, C. F., Barbero, L., Bates, N. R., Bianchi, A. A., Bonou, F., Boutin, J., Bozec, Y., Burger, E. F., Cai, W.-J., Castle, R. D., Chen, L., Chierici, M., Currie, K., Evans, W., Featherstone, C., Feely, R. A., Fransson, A., Goyet, C., Greenwood, N., Gregor, L., Hankin, S., Hardman-Mountford, N. J., Harlay, J., Hauck, J., Hoppema, M., Humphreys, M. P., Hunt, C. W., Huss, B., Ibánhez, J. S. P., Johannessen, T., Keeling, R., Kitidis, V., Körtzinger, A., Kozyr, A., Krasakopoulou, E., Kuwata, A., Landschützer, P., Lauvset, S. K., Lefèvre, N., Lo Monaco, C., Manke, A., Mathis, J. T., Merlivat, L., Millero, F. J., Monteiro, P. M. S., Munro, D. R., Murata, A., Newberger, T., Omar, A. M., Ono, T., Paterson, K., Pearce, D., Pierrot, D., Robbins, L. L., Saito, S., Salisbury, J., Schlitzer, R., Schneider, B., Schweitzer, R., Sieger, R., Skjelvan, I., Sullivan, K. F., Sutherland, S. C., Sutton, A. J., Tadokoro, K., Telszewski, M., Tuma, M., van Heuven, S. M. A. C., Vandemark, D., Ward, B., Watson, A. J., and Xu, S.: A multidecade record of high-quality fCO2 data in version 3 of the Surface Ocean CO2 Atlas (SOCAT), Earth Syst. Sci. Data, 8, 383–413, https://doi.org/10.5194/essd-8-383-2016, 2016.

Batchelor, G. K. and Townsend, A. A.: The Nature of Turbulent Motion at Large Wave-Numbers, P. R. Soc. A: Math. Phy., 199, 238–255, https://doi.org/10.1098/rspa.1949.0136, 1949.

Bestehorn, M., Michelitsch, T. M., Collet, B. A., Riascos, A. P., and Nowakowski, A. F.: Simple Model of Epidemic Dynamics with Memory Effects, Phys. Rev. E, 105, 024205, https://doi.org/10.1103/PhysRevE.105.024205, 2022.

Bozec, Y., Merlivat, L., Baudoux, A. C., Beaumont, L., Blain, S., Bucciarelli, E., Danguy, T., Grossteffan, E., Guillot, A., Guillou, J., Répécaud, M., and Tréguer, P.: Diurnal to Inter-Annual Dynamics of pCO_2 Recorded by a CARIOCA Sensor in a Temperate Coastal Ecosystem (2003–2009), Mar. Chem., 126, 13–26, https://doi.org/10.1016/j.marchem.2011.03.003, 2011.

Bozec, Y., Loisel, S., and Bureau, S.: ASTAN Cardinal Buoy (Western English Channel, France) Data from 2015 to 2019, SEANOE [data set], https://doi.org/10.17882/106537, 2025.

Ciais, P., Dolman, A. J., Bombelli, A., Duren, R., Peregon, A., Rayner, P. J., Miller, C., Gobron, N., Kinderman, G., Marland, G., Gruber, N., Chevallier, F., Andres, R. J., Balsamo, G., Bopp, L., Bréon, F.-M., Broquet, G., Dargaville, R., Battin, T. J., Borges, A., Bovensmann, H., Buchwitz, M., Butler, J., Canadell, J. G., Cook, R. B., DeFries, R., Engelen, R., Gurney, K. R., Heinze, C., Heimann, M., Held, A., Henry, M., Law, B., Luyssaert, S., Miller, J., Moriyama, T., Moulin, C., Myneni, R. B., Nussli, C., Obersteiner, M., Ojima, D., Pan, Y., Paris, J.-D., Piao, S. L., Poulter, B., Plummer, S., Quegan, S., Raymond, P., Reichstein, M., Rivier, L., Sabine, C., Schimel, D., Tarasova, O., Valentini, R., Wang, R., van der Werf, G., Wickland, D., Williams, M., and Zehner, C.: Current systematic carbon-cycle observations and the need for implementing a policy-relevant carbon observing system, Biogeosciences, 11, 3547–3602, https://doi.org/10.5194/bg-11-3547-2014, 2014.

Corrsin, S.: On the Spectrum of Isotropic Temperature Fluctuations in an Isotropic Turbulence, J. Appl. Phys., 22, 469–473, https://doi.org/10.1063/1.1699986, 1951.

Crosswell, J. R., Wetz, M. S., Hales, B., and Paerl, H. W.: Extensive CO_2 Emissions from Shallow Coastal Waters during Passage of Hurricane Irene (August 2011) over the Mid-Atlantic Coast of the USA, Limnol. Oceanogr., 59, 1651–1665, https://doi.org/10.4319/lo.2014.59.5.1651, 2014.

Dauvin, J.-C.: The English Channel: La Manche, in: World Seas: An Environmental Evaluation, 2nd. edn., Chapt. 6, edited by: Sheppard, C., Academic Press, 153–188, https://doi.org/10.1016/B978-0-12-805068-2.00008-5, 2019.

Friedlingstein, P., O'Sullivan, M., Jones, M. W., Andrew, R. M., Bakker, D. C. E., Hauck, J., Landschützer, P., Le Quéré, C., Luijkx, I. T., Peters, G. P., Peters, W., Pongratz, J., Schwingshackl, C., Sitch, S., Canadell, J. G., Ciais, P., Jackson, R. B., Alin, S. R., Anthoni, P., Barbero, L., Bates, N. R., Becker, M., Bellouin, N., Decharme, B., Bopp, L., Brasika, I. B. M., Cadule, P., Chamberlain, M. A., Chandra, N., Chau, T.-T.-T., Chevallier, F., Chini, L. P., Cronin, M., Dou, X., Enyo, K., Evans, W., Falk, S., Feely, R. A., Feng, L., Ford, D. J., Gasser, T., Ghattas, J., Gkritzalis, T., Grassi, G., Gregor, L., Gruber, N., Gürses, Ö., Harris, I., Hefner, M., Heinke, J., Houghton, R. A., Hurtt, G. C., Iida, Y., Ilyina, T., Jacobson, A. R., Jain, A., Jarníková, T., Jersild, A., Jiang, F., Jin, Z., Joos, F., Kato, E., Keeling, R. F., Kennedy, D., Klein Goldewijk, K., Knauer, J., Korsbakken, J. I., Körtzinger, A., Lan, X., Lefèvre, N., Li, H., Liu, J., Liu, Z., Ma, L., Marland, G., Mayot, N., McGuire, P. C., McKinley, G. A., Meyer, G., Morgan, E. J., Munro, D. R., Nakaoka, S.-I., Niwa, Y., O'Brien, K. M., Olsen, A., Omar, A. M., Ono, T., Paulsen, M., Pierrot, D., Pocock, K., Poulter, B., Powis, C. M., Rehder, G., Resplandy, L., Robertson, E., Rödenbeck, C., Rosan, T. M., Schwinger, J., Séférian, R., Smallman, T. L., Smith, S. M., Sospedra-Alfonso, R., Sun, Q., Sutton, A. J., Sweeney, C., Takao, S., Tans, P. P., Tian, H., Tilbrook, B., Tsujino, H., Tubiello, F., van der Werf, G. R., van Ooijen, E., Wanninkhof, R., Watanabe, M., Wimart-Rousseau, C., Yang, D., Yang, X., Yuan, W., Yue, X., Zaehle, S., Zeng, J., and Zheng, B.: Global Carbon Budget 2023, Earth Syst. Sci. Data, 15, 5301–5369, https://doi.org/10.5194/essd-15-5301-2023, 2023.

Frisch, U.: Turbulence: The Legacy of A. N. Kolmogorov, Cambridge University Press, https://doi.org/10.1017/CBO9781139170666, 1995.

Gac, J.-P., Marrec, P., Cariou, T., Guillerm, C., Macé, É., Vernet, M., and Bozec, Y.: Cardinal Buoys: An Opportunity for the Study of Air–Sea CO_2 Fluxes in Coastal Ecosystems, Frontiers in Marine Science, 7, https://doi.org/10.3389/fmars.2020.00712, 2020.

Gao, Y., Schmitt, F. G., Hu, J., and Huang, Y.: Scaling Analysis of the China France Oceanography Satellite Along-Track Wind and Wave Data, J. Geophys. Res.: Oceans, 126, e2020JC017119, https://doi.org/10.1029/2020JC017119, 2021.

Giancaterini, F., Hecq, A., and Morana, C.: Is Climate Change Time-Reversible?, Econometrics, 10, 36, https://doi.org/10.3390/econometrics10040036, 2022.

Huang, N. E., Shen, Z., Long, S. R., Wu, M. C., Shih, H. H., Zheng, Q., Yen, N.-C., Tung, C. C., and Liu, H. H.: The Empirical Mode Decomposition and the Hilbert Spectrum for Nonlinear and Non-Stationary Time Series Analysis, P. R. Soc. A: Math. Phy., 454, 903–995, https://doi.org/10.1098/rspa.1998.0193, 1998.

Hugh-Jones, D.: Ggmagnify: Create a Magnified Inset of Part of a "Ggplot" Object [code], https://hughjonesd.github.io/ggmagnify/ (last access: 17 December 2025), 2023.

Idier, D., Dumas, F., and Muller, H.: Tide-surge interaction in the English Channel, Nat. Hazards Earth Syst. Sci., 12, 3709–3718, https://doi.org/10.5194/nhess-12-3709-2012, 2012.

IPCC: Climate Change 2023: Synthesis Report. Contribution of Working Groups I, II and III to the Sixth Assessment Report of the Intergovernmental Panel on Climate Change, IPCC, Geneva, Switzerland, https://doi.org/10.59327/IPCC/AR6-9789291691647, 2023.

Jiang, L.-Q., Cai, W.-J., Wang, Y., and Bauer, J. E.: Influence of terrestrial inputs on continental shelf carbon dioxide, Biogeosciences, 10, 839–849, https://doi.org/10.5194/bg-10-839-2013, 2013.

Kolmogorov, A. N.: On Degeneration (Decay) of Isotropic Turbulence in an Incompressible Viscous Liquid, Doklady Akademii Nauk SSSR, 31, 538–540, 1941.

Levoy, F., Anthony, E. J., Monfort, O., and Larsonneur, C.: The Morphodynamics of Megatidal Beaches in Normandy, France, Mar. Geol., 171, 39–59, https://doi.org/10.1016/S0025-3227(00)00110-9, 2000.

Marrec, P., Cariou, T., Collin, E., Durand, A., Latimier, M., Macé, E., Morin, P., Raimund, S., Vernet, M., and Bozec, Y.: Seasonal and Latitudinal Variability of the CO_2 System in the Western English Channel Based on Voluntary Observing Ship (VOS) Measurements, Mar. Chem., 155, 29–41, https://doi.org/10.1016/j.marchem.2013.05.014, 2013.

Mathai, J. and Mujumdar, P. P.: Use of streamflow indices to identify the catchment drivers of hydrographs, Hydrol. Earth Syst. Sci., 26, 2019–2033, https://doi.org/10.5194/hess-26-2019-2022, 2022.

Northcott, D., Sevadjian, J., Sancho-Gallegos, D. A., Wahl, C., Friederich, J., and Chavez, F. P.: Impacts of Urban Carbon Dioxide Emissions on Sea-Air Flux and Ocean Acidification in Nearshore Waters, PLOS ONE, 14, e0214403, https://doi.org/10.1371/journal.pone.0214403, 2019.

Obukhov, A. M.: The Structure of the Temperature Field in a Turbulent Flow, Izvestiya Akademii Nauk SSSR. Geografiya i Geofizika, 13, 58–69, 1949.

Pingree, R. D. and Griffiths, D. K.: Tidal Fronts on the Shelf Seas around the British Isles, J. Geophys. Res.: Oceans, 83, 4615–4622, https://doi.org/10.1029/JC083iC09p04615, 1978.

Pomeau, Y.: Symétrie des fluctuations dans le renversement du temps, Journal de Physique, 43, 859–867, https://doi.org/10.1051/jphys:01982004306085900, 1982.

Pomeau, Y.: Time in Science: Reversibility vs. Irreversibility, in: Discrete Integrable Systems, edited by Grammaticos, B., Tamizhmani, T., and Kosmann-Schwarzbach, Y., 425–436, Springer, Berlin, Heidelberg, https://doi.org/10.1007/978-3-540-40357-9_10, 2004.

Reid, P. C., Auger, C., Chaussepied, M., and Burn, M.: Quality Status Report of the North Sea 1993: Report on Sub-region 9: The Channel, North Sea Task Force, UK Dep. of the Environ., Républ. Fr. Minist. de l'Environ., Inst. Fr. de Rech. Pour l'Exploit. de la Mer, Brest, 1993.

Reimer, J. J., Cai, W.-J., Xue, L., Vargas, R., Noakes, S., Hu, X., Signorini, S. R., Mathis, J. T., Feely, R. A., Sutton, A. J., Sabine, C., Musielewicz, S., Chen, B., and Wanninkhof, R.: Time Series pCO_2 at a Coastal Mooring: Internal Consistency, Seasonal Cycles, and Interannual Variability, Cont. Shelf. Res., 145, 95–108, https://doi.org/10.1016/j.csr.2017.06.022, 2017.

Robache, K. and Schmitt, F. G.: Thermal and Non-Thermal Components of pCO_2 Estimated from ASTAN Cardinal Buoy (Western English Channel) Data from 2015 to 2019, SEANOE [data set], https://doi.org/10.17882/106550, 2025.

Robache, K., Schmitt, F. G., and Huang, Y.: Scaling and intermittent properties of oceanic and atmospheric pCO_2 time series and their difference in a turbulence framework, Nonlin. Processes Geophys., 32, 35–49, https://doi.org/10.5194/npg-32-35-2025, 2025.

Schmitt, F. G.: Scaling Analysis of Time-Reversal Asymmetries in Fully Developed Turbulence, Fractal and Fractional, 7, 630, https://doi.org/10.3390/fractalfract7080630, 2023.

Schmitt, F. G. and Huang, Y.: Stochastic Analysis of Scaling Time Series: From Turbulence Theory to Applications, Cambridge University Press, https://doi.org/10.1017/CBO9781107705548, 2016.

Séférian, R., Bopp, L., Swingedouw, D., and Servonnat, J.: Dynamical and biogeochemical control on the decadal variability of ocean carbon fluxes, Earth Syst. Dynam., 4, 109–127, https://doi.org/10.5194/esd-4-109-2013, 2013.

Seuront, L., Schmitt, F., Lagadeuc, Y., Schertzer, D., Lovejoy, S., and Frontier, S.: Multifractal Analysis of Phytoplankton Biomass and Temperature in the Ocean, Geophys. Res. Lett., 23, 3591–3594, https://doi.org/10.1029/96GL03473, 1996.

Simboura, N., Panayotidis, P., and Papathanassiou, E.: A Synthesis of the Biological Quality Elements for the Implementation of the European Water Framework Directive in the Mediterranean Ecoregion: The Case of Saronikos Gulf, Ecol. Indic., 5, 253–266, https://doi.org/10.1016/j.ecolind.2005.03.006, 2005.

Sutton, A. J., Sabine, C. L., Maenner-Jones, S., Lawrence-Slavas, N., Meinig, C., Feely, R. A., Mathis, J. T., Musielewicz, S., Bott, R., McLain, P. D., Fought, H. J., and Kozyr, A.: A high-frequency atmospheric and seawater pCO_2 data set from 14 open-ocean sites using a moored autonomous system, Earth Syst. Sci. Data, 6, 353–366, https://doi.org/10.5194/essd-6-353-2014, 2014.

Sutton, A. J., Feely, R. A., Maenner-Jones, S., Musielwicz, S., Osborne, J., Dietrich, C., Monacci, N., Cross, J., Bott, R., Kozyr, A., Andersson, A. J., Bates, N. R., Cai, W.-J., Cronin, M. F., De Carlo, E. H., Hales, B., Howden, S. D., Lee, C. M., Manzello, D. P., McPhaden, M. J., Meléndez, M., Mickett, J. B., Newton, J. A., Noakes, S. E., Noh, J. H., Olafsdottir, S. R., Salisbury, J. E., Send, U., Trull, T. W., Vandemark, D. C., and Weller, R. A.: Autonomous seawater pCO_2 and pH time series from 40 surface buoys and the emergence of anthropogenic trends, Earth Syst. Sci. Data, 11, 421–439, https://doi.org/10.5194/essd-11-421-2019, 2019.

Takahashi, T., Olafsson, J., Goddard, J. G., Chipman, D. W., and Sutherland, S. C.: Seasonal Variation of CO_2 and Nutrients in the High-Latitude Surface Oceans: A Comparative Study, Global Biogeochem. Cy., 7, 843–878, https://doi.org/10.1029/93GB02263, 1993.

Takahashi, T., Sutherland, S. C., Sweeney, C., Poisson, A., Metzl, N., Tilbrook, B., Bates, N., Wanninkhof, R., Feely, R. A., Sabine, C., Olafsson, J., and Nojiri, Y.: Global Sea–Air CO_2 Flux Based on Climatological Surface Ocean pCO_2, and Seasonal Biological and Temperature Effects, Deep-Sea Res. Pt. II, 49, 1601–1622, https://doi.org/10.1016/S0967-0645(02)00003-6, 2002.

Takahashi, T., Sutherland, S. C., Wanninkhof, R., Sweeney, C., Feely, R. A., Chipman, D. W., Hales, B., Friederich, G., Chavez, F., Sabine, C., Watson, A., Bakker, D. C. E., Schuster, U., Metzl, N., Yoshikawa-Inoue, H., Ishii, M., Midorikawa, T., Nojiri, Y., Körtzinger, A., Steinhoff, T., Hoppema, M., Olafsson, J., Arnarson, T. S., Tilbrook, B., Johannessen, T., Olsen, A., Bellerby, R., Wong, C. S., Delille, B., Bates, N. R., and de Baar, H. J. W.: Climatological Mean and Decadal Change in Surface Ocean pCO_2, and Net Sea–Air CO_2 Flux over the Global Oceans, Deep-Sea Res. Pt. II, 56, 554–577, https://doi.org/10.1016/j.dsr2.2008.12.009, 2009.

Torres, O., Kwiatkowski, L., Sutton, A. J., Dorey, N., and Orr, J. C.: Characterizing Mean and Extreme Diurnal Variability of Ocean CO_2 System Variables Across Marine Environments, Geophys. Res. Lett., 48, e2020GL090228, https://doi.org/10.1029/2020GL090228, 2021.

Wand, M. P. and Jones, M. C.: Kernel Smoothing, CRC Press, https://doi.org/10.1201/b14876, 1994.

Wanninkhof, R., Pierrot, D., Sullivan, K., Mears, P., and Barbero, L.: Comparison of Discrete and Underway CO_2 Measurements: Inferences on the Temperature Dependence of the Fugacity of CO_2 in Seawater, Mar. Chem., 247, 104178, https://doi.org/10.1016/j.marchem.2022.104178, 2022.

Weiss, R. F.: The Solubility of Nitrogen, Oxygen and Argon in Water and Seawater, Deep Sea Research and Oceanographic Abstracts, 17, 721–735, https://doi.org/10.1016/0011-7471(70)90037-9, 1970.

Wickham, H. and RStudio: Tidyverse: Easily Install and Load the "Tidyverse", Version 2.0.0, CRAN [code], https://doi.org/10.32614/CRAN.package.tidyverse, 2023.

Wickham, H., Averick, M., Bryan, J., Chang, W., McGowan, L. D., François, R., Grolemund, G., Hayes, A., Henry, L., Hester, J., Kuhn, M., Pedersen, T. L., Miller, E., Bache, S. M., Müller, K., Ooms, J., Robinson, D., Seidel, D. P., Spinu, V., Takahashi, K., Vaughan, D., Wilke, C., Woo, K., and Yutani, H.: Welcome to the Tidyverse, Journal of Open Source Software, 4, 1686, https://doi.org/10.21105/joss.01686, 2019.

Wickham, H., Chang, W., Henry, L., Pedersen, T. L., Takahashi, K., Wilke, C., Woo, K., Yutani, H., Dunnington, D., van den Brand, T., Posit, and PBC: Ggplot2: Create Elegant Data Visualisations Using the Grammar of Graphics, Version 3.5.1, CRAN [code], https://doi.org/10.32614/CRAN.package.ggplot2, 2025.

Wimart-Rousseau, C., Lajaunie-Salla, K., Marrec, P., Wagener, T., Raimbault, P., Lagadec, V., Lafont, M., Garcia, N., Diaz, F., Pinazo, C., Yohia, C., Garcia, F., Xueref-Remy, I., Blanc, P.-E., Armengaud, A., and Lefèvre, D.: Temporal Variability of the Carbonate System and Air–Sea CO_2 Exchanges in a Mediterranean Human-Impacted Coastal Site, Estuar. Coast. Shelf S., 236, 106641, https://doi.org/10.1016/j.ecss.2020.106641, 2020.

Xu, H., Ouellette, N. T., and Bodenschatz, E.: Curvature of Lagrangian Trajectories in Turbulence, Phys. Rev. Lett., 98, 050201, https://doi.org/10.1103/PhysRevLett.98.050201, 2007.

Yu, P., Wang, Z. A., Churchill, J., Zheng, M., Pan, J., Bai, Y., and Liang, C.: Effects of Typhoons on Surface Seawater pCO_2 and Air–Sea CO_2 Fluxes in the Northern South China Sea, J. Geophys. Res.: Oceans, 125, e2020JC016258, https://doi.org/10.1029/2020JC016258, 2020.

Zongo, S. B. and Schmitt, F. G.: Scaling properties of pH fluctuations in coastal waters of the English Channel: pH as a turbulent active scalar, Nonlin. Processes Geophys., 18, 829–839, https://doi.org/10.5194/npg-18-829-2011, 2011.